

# Latest results of the ALICE Collaboration and plans for ALICE 3

A. Marin, for the ALICE Collaboration

GSI Helmholtzzentrum für Schwerionenforschung GmbH, Planckstrasse 1, 64291 Darmstadt, Germany

Received June 21, 2023; accepted DD MM 2023

The ALICE experiment is devoted to the study of the quark-gluon plasma (QGP) created in heavy-ion collisions at the CERN LHC. The experimental setup allows for the study of many different observables that contributed to the characterization of the properties of the QGP. The ALICE experiment went through a major upgrade during LS2 to profit from the increased LHC luminosity and to improve the tracking resolution. An additional upgrade is planned for LS3. A new experiment, ALICE 3, was proposed as next major upgrade in LS4. In this contribution, a selection of recent physics results was presented together with a glimpse of the next upgrades during LS3 and LS4, with the main focus on ALICE 3 and its physics program.

**Keywords:** QGP, heavy-ion, LHC, ALICE, ALICE 3

## 1 Introduction

Heavy-ion collisions at ultrarelativistic energies allow to explore the phase diagram of QCD matter. Lattice QCD calculations predict that a state of matter where quarks and gluons are deconfined, known as the QGP, is produced above a given energy density. In order to characterize the QGP several probes can be used, each of them being sensitive to different properties. Furthermore, the complete evolution of the heavy-ion collision is studied, from the pre-equilibrium phase, the QGP phase, hydrodynamical expansion and hadron gas phase up to the kinetic and thermal freeze-out.

Figure 1 displays the ALICE experiment at the CERN LHC during Run 2. The description of the apparatus and its performance can be found in Refs. [1, 2]. The LHC schedule with the different data taking runs, shutdown periods and ALICE configurations is shown in Fig. 2.

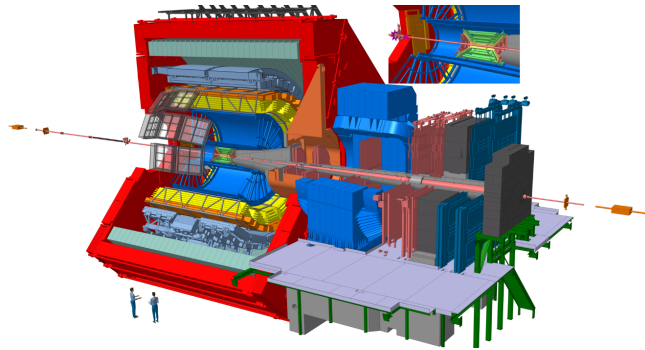


FIGURE 1. Schematic view of the ALICE apparatus during Run 2.

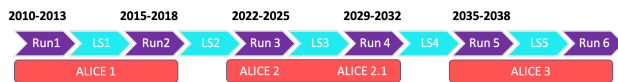


FIGURE 2. LHC schedule with the different data taking runs, shutdown periods and ALICE configurations.

The ALICE collaboration consists of more than 2000 people distributed over more than 175 institutes in about 40

countries. A large number of physics results was published in more than 400 papers. A review of the most important results was made available recently [3]. In the following, few selected recent results will be described. Furthermore, some details on the already started Run 3 are given as well as a glimpse of the future upgrades and the physics program.

## 2 Global properties

The multiplicity of charged particles produced at mid-rapidity in heavy-ion collisions is a key observable to characterize the properties of the matter created in these collisions. The dependence of  $dN_{ch}/d\eta$  on collision system, center-of-mass energy and collision geometry are basic observables for understanding the different particle production mechanisms. ALICE measured a power law dependence on the charged particle multiplicity density as a function of the center of mass energy per nucleon pair in pp and Pb–Pb collisions [4]. A larger exponent for nuclear collisions as compared to pp collisions evidences that more energy is available for particle production in these collisions compared to pp.

One of the strengths of ALICE is its particle identification capabilities as a result of using most of the available techniques and the low transverse momentum ( $p_T$ ) reach. Thus, a broad set of high precision measurements of identified particles differentially as a function of transverse momentum and collision centrality were carried out in pp, p–Pb and Pb–Pb collisions [5]. The spectra become flatter with increasing charged particle multiplicity, the effect being more pronounced for heavier particles. The low  $p_T$  spectra were parametrized with blast-wave fits across the systems obtaining freeze-out temperature  $T_{kin}$  and radial flow velocities  $\beta_T$  that depend strongly on  $dN_{ch}/d\eta$  [6]. With all these differential measurements, computed integrated yields of different particle species with respect to those of charged pions were studied as a function of charged particle multiplicity with the main focus on strange and multistrange particles [7] as strangeness enhancement was proposed as a signature of QGP formation in nuclear collisions. A continuous evolution of strangeness production between different colli-

sion systems and energies is observed. The magnitude of the strangeness enhancement grows with the strange quark content. The hadron yields are mostly related to the final state charged particle multiplicity density rather than collision system or beam energy. Furthermore, multiplicities of hadron species containing only light quarks measured at midrapidity in central Pb–Pb collisions, spanning over nine orders of magnitude in abundance values, are well described by statistical hadronization models [3].

Studies of the azimuthal anisotropy of particle production have contributed significantly to the characterization of the system created in heavy-ion collisions. Anisotropic flow reflects the conversion of the initial state spatial anisotropy into final state anisotropies in momentum space. Elliptic flow in Pb–Pb, p–Pb and pp collision was measured [8] using two ( $v_2\{2\}$ ) and four-particle ( $v_2\{4\}$ ) cumulants for different particle species. A mass ordering was found at low  $p_T$ , and at intermediate  $p_T$  baryon vs meson grouping that can be interpreted as quark-level flow and recombination. Models including quark coalescence describe the measurements over a large  $p_T$  range, which confirms the relevance of the quark coalescence hadronization mechanism in the particle production in pp, p–Pb and Pb–Pb collisions at the LHC.

Viscous hydrodynamic calculations using various initial state models were able to describe multiplicity distributions, particle momentum spectra and integrated flow measurements. Uncertainties in the initial state translated into large uncertainties on the extracted shear viscosity over entropy ratio,  $\eta/s$ , value. Some progress was achieved in the last years. Novel approaches utilizing Bayesian statistics and a multi-parameter model-to-data comparison of different observables like multiplicity, transverse momentum, and flow are used to quantitatively extract estimates of the temperature-dependent specific shear and bulk viscosity simultaneously with related initial-condition properties [9] or to characterize additional aspects of high-energy nuclear collisions [10].

Correlations of  $v_2$  vs mean  $p_T$ ,  $\rho(v_n^2, [p_T])$ , as a function of centrality (Fig. 3) are mainly driven by the correlations of

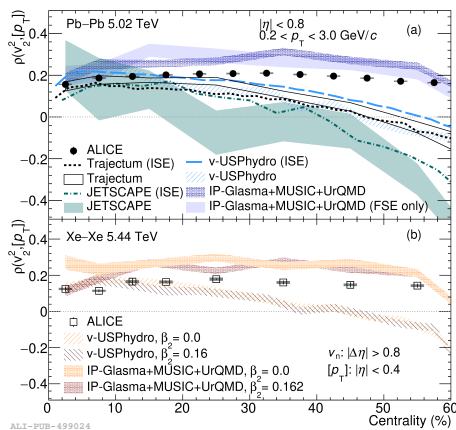


FIGURE 3. Centrality dependence of  $\rho(v_n^2, [p_T])$  in Pb–Pb and Xe–Xe collisions at  $\sqrt{s_{NN}} = 5.02$  TeV and  $\sqrt{s_{NN}} = 5.44$  TeV, respectively, compared to different model calculations.

the size and the shape of the system in the initial state, and as such provide a novel way to characterize the initial state and help pin down the uncertainty of the extracted properties of the quark–gluon plasma. The sensitivity of the correlations of  $v_2$  vs mean  $p_T$  vs centrality,  $\rho(v_n^2, [p_T])$  to the initial conditions can be observed in Fig. 3 [11]. Data for Pb–Pb and Xe–Xe collisions are closer to IP-Glasma initial condition as compared to Trento initial conditions. Therefore, including measurements of  $\rho(v_n^2, [p_T])$  vs centrality in Bayesian global fitting approaches could result in better constraint on the initial state in nuclear collisions.

The two-particle transverse momentum correlator  $G_2$  was proposed [12, 13] because of its sensitivity to the transport characteristics of the QGP. The longitudinal width evolution with collision centrality carries information about  $\eta/s$  [14], while it does not have any explicit dependence on the initial state fluctuations in the transverse plane of the system. The  $G_2$  width evolution measured as a function of centrality in Pb–Pb collisions at  $\sqrt{s_{NN}} = 2.76$  TeV [15] (Fig. 4) favours small values of  $\eta/s$  at LHC energies. Furthermore, no evidence for shear viscous effects was found in pp and p–Pb collisions based on  $G_2$  (Fig. 5), or the system lifetime was too short for viscous forces to play a significant role [16].

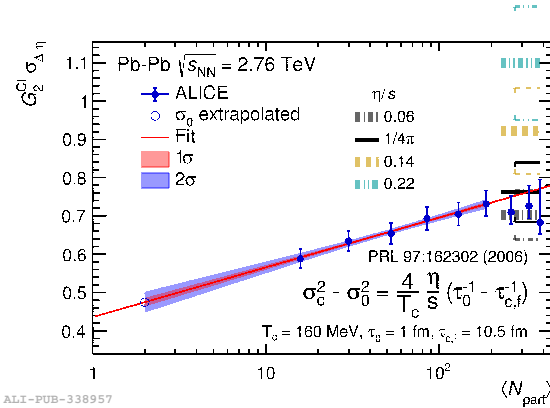


FIGURE 4. Width of  $G_2$  in  $\Delta\eta$  as a function of  $\langle N_{part} \rangle$  for Pb–Pb collisions at  $\sqrt{s_{NN}} = 2.76$  TeV.

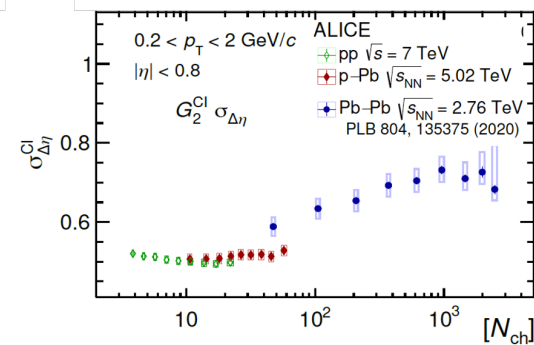


FIGURE 5. Width of  $G_2$  in  $\Delta\eta$  as a function of charge particle multiplicity for pp, p–Pb and Pb–Pb collisions.

ALICE data on the longitudinal width of  $G_2$  were used to

compute values of  $\eta/s$  as a function of the charged particle multiplicity, obtaining  $\eta/s$  values in the range from  $0.04 \pm 0.02$  (sys) to  $0.07 \pm 0.03$ (sys) for LHC energies [17].

### 3 Electromagnetic radiation

Photons and dileptons (lepton-antilepton pairs from internal conversion of virtual photons) are produced throughout all stages of the collisions. They are unique probes of the QGP because they leave the medium unaffected by the strong interaction. They provide information about the temperature and the radial expansion velocity of the QGP.

Dileptons carry mass that can be used to distinguish between different sources of the radiation, and which allows for temperature measurements without a blue shift. At low invariant mass ( $m_{ee} < 1.1$  GeV/ $c^2$ ), the dielectron production is sensitive to the properties of short-lived vector mesons in the medium related to chiral symmetry restoration ( $\rho$ - $a_1$ , vector-axial vector meson mixing). The intermediate-mass region ( $1.2$  GeV/ $c^2 < m_{ee} < 2.7$  GeV/ $c^2$ ), is where the thermal blackbody radiation dominates and the early temperature of the system can be extracted after subtraction of the very large background of correlated dielectron pairs from semi-leptonic charm and beauty hadron decays. Fig. 6 shows the dielectron invariant mass distribution for central 0-10% Pb-Pb collisions at  $\sqrt{s_{NN}} = 5.02$  TeV compared to the hadronic cocktail for two different versions of the correlated background from heavy flavour hadron decays. Middle and bottom plots show the respective ratio to the cocktails excluding the vacuum  $\rho$ .

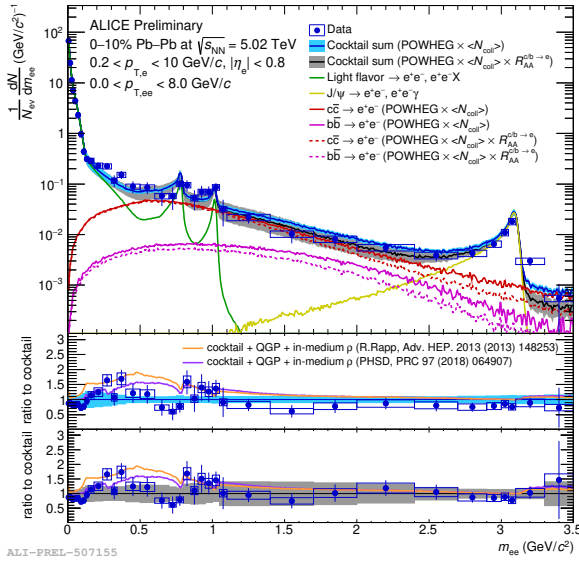


FIGURE 6. Dielectron invariant mass distribution for central 0-10% Pb-Pb collisions at  $\sqrt{s_{NN}} = 5.02$  TeV compared to the hadronic cocktail for two different versions of the correlated background from heavy flavour hadron decays. Middle and bottom plots show the respective ratio to the cocktails excluding the vacuum  $\rho$ .

Data show an indication for an excess at lower mass com-

patible with the thermal radiation from the partonic and hadronic gas phase [18, 19] up to  $m_{ee} < 0.5$  GeV/ $c^2$  while the model calculations overestimate the data for  $0.5 < m_{ee} < 0.7$  GeV/ $c^2$ . The intermediate mass region agrees better with the expectations of the models for the cocktail including HF suppression [20].

Direct photons are photons not coming from hadronic decays. Experimentally, they can be measured using a double ratio  $R_\gamma$  defined as

$$R_\gamma = \frac{(N_{\gamma,inc}/N_{\pi^0})_{measured}}{(N_{\gamma,decay}/N_{\pi^0})_{sim}} \quad (1)$$

in order to cancel correlated uncertainties. The decay photon spectra are estimated employing the decay cocktail framework [21] using as input the measured  $\pi^0$  and  $\eta$  meson spectra and  $m_T$  scaling for non measured spectra. The  $R_\gamma$  as a function of  $p_T$  is shown in Fig. 7 from central (top) to peripheral (bottom) Pb-Pb collisions at  $\sqrt{s_{NN}} = 5.02$  TeV.

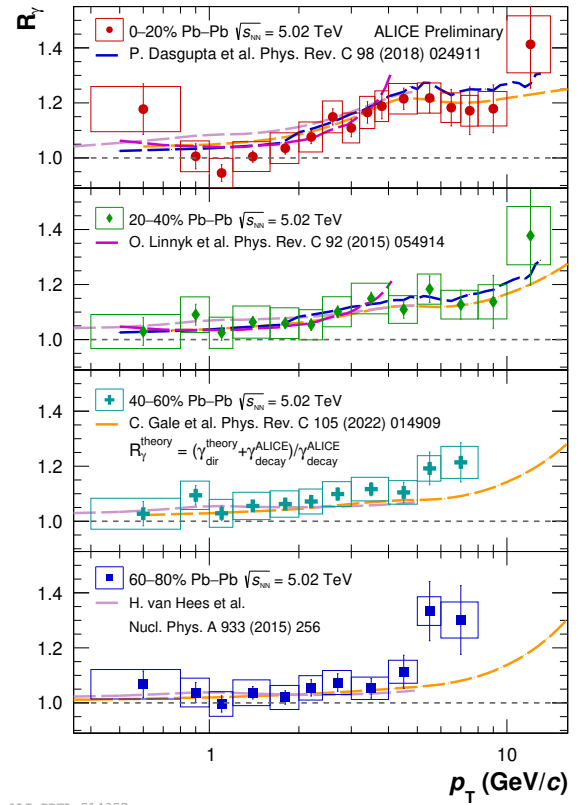


FIGURE 7.  $R_\gamma$  as a function of  $p_T$  from central (top) to peripheral (bottom) Pb-Pb collisions at  $\sqrt{s_{NN}} = 5.02$  TeV together with expectations from model calculations that include thermal photons, (and pre-equilibrium photon) and prompt photons.

At low  $p_T$  where the thermal radiation dominates the measurement the value of  $R_\gamma$  is close to 1, which entails a small contribution from thermal and pre-equilibrium photons. For  $p_T > 3$  GeV/ $c$ , a value of  $R_\gamma > 1$  is measured which is attributed to prompt photons from hard scatterings. At low  $p_T$ , model calculations with thermal and pre-equilibrium

photons agree better with the data than if only prompt photons [22] are included. Several model calculations that contain different assumptions (microscopic transport approach or relativistic hydrodynamic with different initial conditions, thermalization times with and without pre-equilibrium photons) are able to describe the data. The current uncertainties do not allow for discrimination among the different theoretical model calculations [22–31]. More precise results are expected with the full Run 2 and Run 3 data.

## 4 Quarkonia

Quarkonia are flavorless mesons whose constituents are a heavy quark and its own antiquark ( $c\bar{c}$  or  $b\bar{b}$  for charmonium or bottomonium, respectively). Most of the states are stable with respect to strong decay into open charm or open bottom because of the mass threshold. In the late 80s, it was realised that colour screening prevents  $c\bar{c}$  binding in a deconfined medium [32]. Consequently, the observation of  $J/\psi$  suppression would provide a signature of QGP formation. Furthermore, the sequential suppression of the different quarkonia states would deliver information about the  $T$  of the QGP [33–35]. Later, it was realised that another mechanism, the (re)generation, will compensate the suppression once the charm quark multiplicity would become sizeable [36–38]. The measured  $J/\psi$   $R_{AA}$  as a function of  $p_T$  for the central and forward rapidity regions in central Pb–Pb collisions at  $\sqrt{s_{NN}} = 5.02$  TeV is displayed in Fig. 8 compared to the TH-TAMU and SHM model calculations [33].  $R_{AA}$  is higher at midrapidity than at forward rapidity for  $p_T < 3$  GeV/c in the most central collisions as can be explained by a large contribution from (re)generation to the  $J/\psi$  yields.

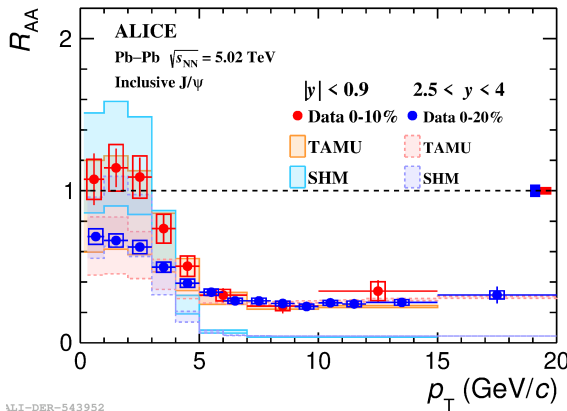


FIGURE 8.  $R_{AA}$  for  $J/\psi$  as a function of  $p_T$  for the central and forward rapidity regions in Pb–Pb collisions at  $\sqrt{s_{NN}} = 5.02$  TeV compared to TH-TAMU and SHM model calculations.

The first accurate measurement of the inclusive  $\Psi(2S)$  down to zero  $p_T$  for  $2.4 < y < 4$  has been achieved by ALICE [39]. Fig. 9 displays the  $p_T$ -dependent  $\Psi(2S)$   $R_{AA}$  compared to the  $J/\psi$   $R_{AA}$ . The  $\Psi(2S)$  has ten times lower binding energy and shows two times larger suppression at low  $p_T$

as compared to the  $J/\psi$ . The strong increase of  $R_{AA}$  towards low  $p_T$  for both quarkonia states is an indication of (re)generation. The ALICE results are in good agreement with CMS results and with theoretical model calculations.

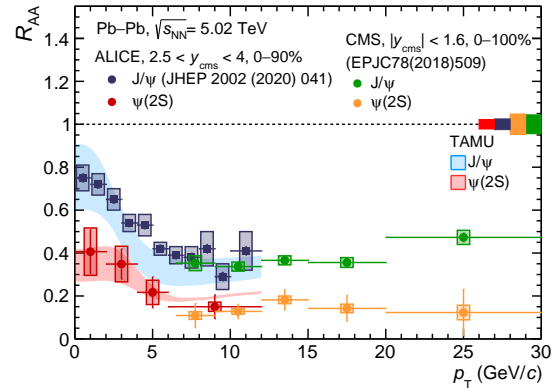


FIGURE 9.  $R_{AA}$  for  $\Psi(2S)$  and  $J/\psi$  as a function of  $p_T$  in Pb–Pb collisions at  $\sqrt{s_{NN}} = 5.02$  TeV compared with theoretical model calculations and results from the CMS experiment.

## 5 Open heavy flavour

Heavy quarks are interesting probes to characterize the QGP, because due to their large mass the production even at low  $p_T$  is driven by hard scatterings in the early stages of the collision and additional thermal production is negligible.

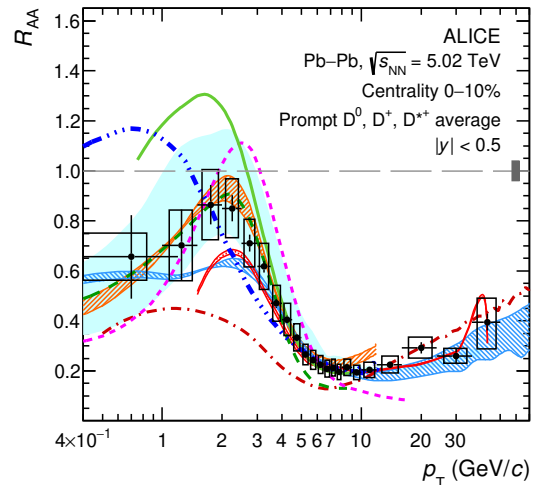


FIGURE 10. Average  $R_{AA}$  of prompt  $D^0$ ,  $D^+$ , and  $D^{++}$  mesons in the 0–10% centrality class in Pb–Pb collisions at  $\sqrt{s_{NN}} = 5.02$  TeV compared with predictions of models implementing charm-quark transport in a hydrodynamically expanding medium.

Thus, heavy quarks experience the full space-time evolution of the hot and dense QCD medium. At low  $p_T$ , heavy-quarks undergo Brownian motion in the medium, carrying, hence,

information of the equilibration process. High  $p_T$  heavy quarks interact with the QGP and lose energy via inelastic (radiative) processes. Open heavy flavor can be measured in ALICE through various channels. Some hadronic decay channels can be fully reconstructed to zero  $p_T$ .

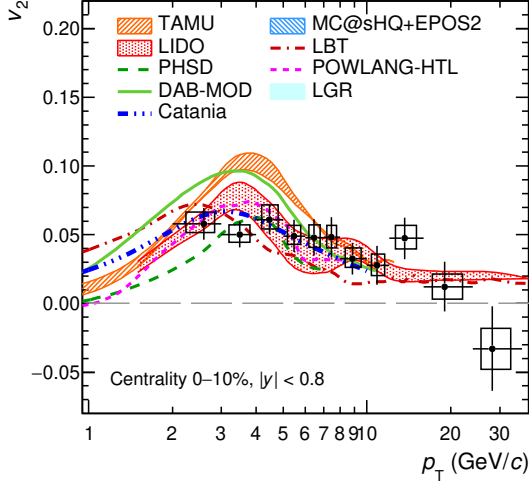


FIGURE 11. Average elliptic flow  $v_2$  of prompt  $D^0$ ,  $D^+$ , and  $D^{*+}$  mesons in the 0–10% centrality class in Pb–Pb collisions at  $\sqrt{s_{NN}} = 5.02$  TeV compared with predictions of models implementing the charm-quark transport in a hydrodynamically expanding medium.

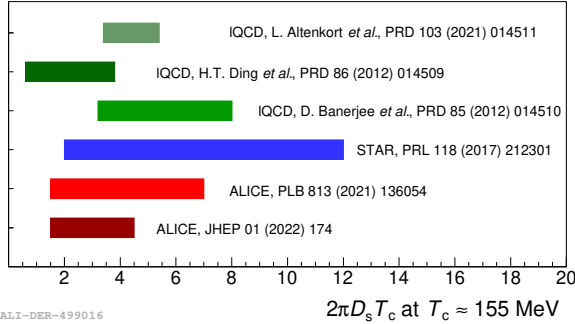


FIGURE 12. Compilation of values for the spatial diffusion coefficient  $D_s$  with their respective uncertainties as obtained by measurements and model calculations.

The average  $R_{AA}$  of prompt  $D^0$ ,  $D^+$ , and  $D^{*+}$  mesons for Pb–Pb collisions in the 0–10% centrality class is shown in Fig. 10 [40]. Compared to the  $R_{AA}$  of charged pions it is larger for  $p_T < 8$  GeV/c. All models shown in Fig. 10 agree with the data, with some tension at low  $p_T$ . The comparison of D-meson  $R_{AA}$  and  $v_2$  (Fig. 11) to models implementing charm-quark transport in a hydrodynamically expanding medium gives information of the interaction of heavy quarks with the medium, constraining the spatial diffusion coefficient. The resulting spatial diffusion coefficient  $D_s$  extracted

from the ALICE measurement ( $1.5 < 2\pi D_s T_c < 4.5$ ) together with a compilation of the values as obtained from measurements and model calculations is shown in Fig. 12. This value of  $D_s$  translates into a relaxation time of the charm quark  $\tau_{charm} \sim 3\text{--}8$  fm/c.

## 6 Jets

The production of jets, i.e. collimated sprays of particles arising from fragmentation of partons produced in high  $Q^2$  interactions, in pp collisions can be well described in pQCD calculations. Thus, by measuring jet suppression in Pb–Pb collisions over a wide set of parameters, properties of the QGP can be extracted.

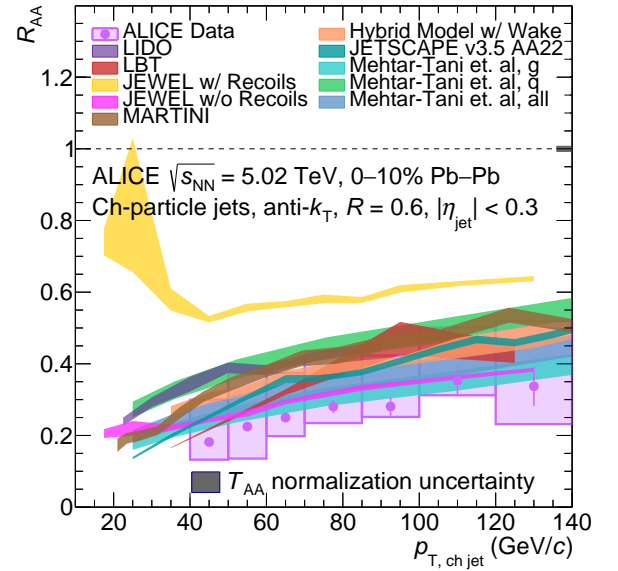


FIGURE 13. Nuclear modification factor ( $R_{AA}$ ) for charged particle jets with  $R=0.6$  obtained using the ML-based method compared to different model predictions [41].

Jet suppression is quantified using the  $R_{AA}$  with a novel machine learning (ML) based approach to subtract underlying Pb–Pb event fluctuations from jet energy (see Fig.13) that allows measurements at transverse momenta as low as 40 GeV/c for a large resolution parameter of  $R = 0.6$  in most central Pb–Pb collisions (or  $p_T > 20$  GeV/c for  $R = 0.2$ ) [41]. A large suppression is still present for  $R = 0.6$  implying that the lost energy is still not recovered within the jet "cone". A comparison of  $R_{AA}$  for  $R = 0.6$  and  $R = 0.2$  indicates that the suppression may be even larger for large-cone ( $R = 0.6$ ) low- $p_T$  jets. The larger acceptance achieved both in  $p_T$  and resolution parameter  $R$ , thanks to the ML-based approach, is crucial for discriminating among different models. A comparison of model calculations to the jet  $R_{AA}$  is shown in Fig. 13). The calculations generally describe the data in central collisions for the smaller resolution parameters ( $R = 0.2$  and 0.4). JEWEL with recoils predicts significantly higher values for  $R_{AA}$  at  $R = 0.6$  than measured.

## 7 ALICE in Run 3 and Run 4 at the LHC

ALICE went through a major upgrade during the LS2 which enables data taking in a continuous readout mode to profit from the increased LHC luminosity and improves the tracking resolution [42]. The upgrades comprise a new inner tracking system (ITS2), new GEM-based readout chambers of the time projection chamber, new muon forward tracker (MFT), new trigger and readout and a new online/offline (O2) software [43].

On July 5, 2022, LHC Run 3 started officially: proton beams collide now at a center of mass energy of 13.6 TeV, the highest energy ever reached. Commissioning with pilot beams during 2021 showed the expected performance of the upgraded experiment in terms of tracking and particle identification (see Fig. 14). A total integrated luminosity of  $15 \text{ pb}^{-1}$  was recorded during 2022 at different interaction rates ranging from 3 kHz up to 1 MHz. Additionally, a test run with Pb beams at  $\sqrt{s_{NN}} = 5.36 \text{ TeV}$  took place prior to the winter break that is crucial to prepare and optimize the data processing and compression. During the upcoming LS3 (see Fig. 2), the FoCal detector [44] will be installed and the current ITS2 will be replaced by the ITS3 [45].

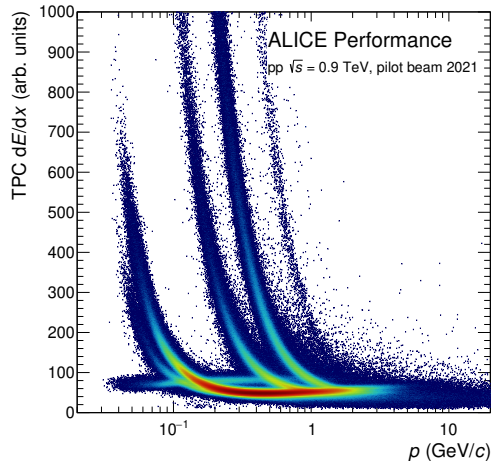


FIGURE 14. Specific energy loss ( $dE/dx$ ) in the TPC versus momentum for pp collisions at  $\sqrt{s} = 0.9 \text{ TeV}$  during the 2021 pilot beam.

## 8 ALICE 3 for Run 5 and Run 6

A huge progress on the characterization of the QGP was already achieved thanks to ALICE results in Run 1 and Run 2, and will continue to deepen with the Run 3 and Run 4 scientific program. However, several essential questions like the fundamental properties of the quark-gluon plasma driving its constituents to equilibration, a comprehensive study of the QGP hadronization mechanisms, the partonic equation of state and its temperature dependence and the underlying dynamics of chiral symmetry restoration will still remain

unanswered after Run 3 and Run 4. Thus, the ALICE Collaboration proposed to install a next generation multipurpose detector, ALICE 3 [46,47], for Run 5 and Run 6 (see Fig. 2).

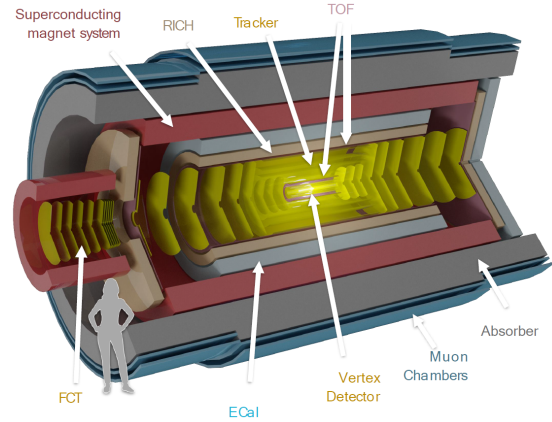


FIGURE 15. Schematic view of the ALICE 3 experiment with the inner and outer trackers, RICH, TOF detectors, ECal and muon detectors in the central and forward/backward barrels, and the forward conversion tracker (FCT) specialized in low momentum photons.

ALICE 3 (see Fig. 15) is based on the use of monolithic active pixel sensors (MAPS) in combination with deep submicron commercial CMOS technologies. The rate capabilities would be a factor of about 50 higher with respect to ALICE in Run 4, being able to exploit the whole delivered p-A and A-A luminosities. ALICE 3 is a large acceptance detector, covering a pseudorapidity range of  $|\eta| < 4$  and  $p_T > 0.02 \text{ GeV}/c$ . The expected track point resolution is  $\sigma_{DCA} \sim 10 \mu\text{m}$  at a  $p_T = 0.2 \text{ GeV}/c$ . The detector will deliver particle identification for  $\gamma$ ,  $e^\pm$ ,  $\mu^\pm$ ,  $K^\pm$  and  $\pi^\pm$ . Such an experiment will be able to deliver systematic measurements of (multi)heavy-flavoured hadrons down to low  $p_T$ , precision differential measurements of dileptons complemented with direct photon measurements, as well as correlation and fluctuation measurements over a large rapidity range among others.

The double-differential analysis of dilepton production in transverse momentum and mass provides access to the time evolution of the temperature. The excellent capabilities of ALICE 3 in terms of good  $e$ -PID down to low  $p_T$ , small detector material budget ( $\gamma$  background) and an excellent pointing resolution (heavy-flavour decay electrons), translate into the expected invariant mass spectrum of thermal  $e^+e^-$  pairs produced in central Pb-Pb collisions at  $\sqrt{s_{NN}} = 5.02 \text{ TeV}$  as depicted in Fig. 16. It would be possible to probe the time dependence of the QGP temperature by fitting the thermal dielectron  $m_{ee}$  spectrum for  $m_{ee} > 1.1 \text{ GeV}/c^2$  (QGP radiation dominated) in bins on pair  $p_{T,ee}$  with

$$\frac{dN_{ee}}{dm_{ee}} \propto (m_{ee}T)^{3/2} e^{-m_{ee}T}. \quad (2)$$

The thermal dielectron elliptic flow as a function of  $m_{ee}$  and  $p_{T,ee}$  would be within reach with ALICE 3. Furthermore,

the high precision thermal dielectron spectrum at  $m_{ee} < 1.2$   $\text{GeV}/c^2$  allows to access the chiral symmetry restoration effects like the  $\rho$ - $a_1$  mixing [18, 47, 48].

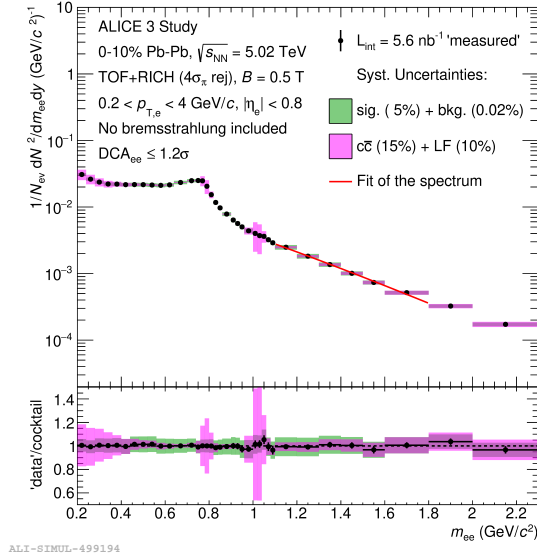


FIGURE 16. Dielectron invariant mass spectrum ( $m_{ee}$ ) fitted with Eq. 2 for  $m_{ee} > 1.1$   $\text{GeV}/c^2$ .

Real photons will be measured in ALICE 3 with the photon conversion method (PCM) and with the electromagnetic

calorimeter (ECAL). The excellent tracking of photon conversion products together with the large acceptance will allow high precision measurements of  $\pi^0$  and  $\eta$  down to zero  $p_T$  reducing the systematic uncertainties of the dominant photon background sources and, therefore, of the direct photon measurements. ALICE 3 will then improve on the measurements of the temperature and elliptic flow of direct photons. By combining the information of real and virtual photons the temperature and the radial expansion velocity of the QGP can be determined.

## 9 Conclusions

Much progress on the characterization of the QGP was achieved thanks to ALICE results in LHC Run 1 and Run 2. Some of the questions that remained open mainly due to statistics will be addressed during the already ongoing Run 3 and Run 4. Others will have to be postponed to Run 5 and Run 6 with the completely new ALICE 3 experiment.

## Acknowledgements

The author would like to thank the organizers for the invitation to present an overview of the ALICE results. I am very grateful for the fruitful discussions and warm atmosphere during the workshop.

1. K. Aamodt et al., The ALICE experiment at the CERN LHC, JINST 3 (2008) S08002, 10.1088/1748-0221/3/08/S08002
2. B. Abelev et al., Performance of the ALICE Experiment at the CERN LHC, Int. J. Mod. Phys. A29 (2014) 1430044, 10.1142/S0217751X14300440
3. The ALICE experiment – A journey through QCD (2022), <https://doi.org/10.48550/arXiv.2211.04384>
4. J. Adam et al., Centrality Dependence of the Charged-Particle Multiplicity Density at Midrapidity in Pb-Pb Collisions at  $\sqrt{s_{NN}} = 5.02$  TeV, Phys. Rev. Lett. 116 (2016) 222302, 10.1103/PhysRevLett.116.222302
5. S. Acharya et al., Production of charged pions, kaons, and (anti-)protons in Pb-Pb and inelastic  $pp$  collisions at  $\sqrt{s_{NN}} = 5.02$  TeV, Phys. Rev. C 101 (2020) 044907, 10.1103/PhysRevC.101.044907
6. S. Acharya et al., Multiplicity dependence of  $\pi$ , K, and p production in  $pp$  collisions at  $\sqrt{s} = 13$  TeV, Eur. Phys. J. C 80 (2020) 693, 10.1140/epjc/s10052-020-8125-1
7. J. Adam et al., Enhanced production of multi-strange hadrons in high-multiplicity proton-proton collisions, Nature Phys. 13 (2017) 535, 10.1038/nphys4111
8. Anisotropic flow and flow fluctuations of identified hadrons in Pb-Pb collisions at  $\sqrt{s_{NN}} = 5.02$  TeV (2022), <https://doi.org/10.48550/arXiv.2206.04587>
9. J. E. Bernhard, J. S. Moreland, and S. A. Bass, Bayesian estimation of the specific shear and bulk viscosity of quark-gluon plasma, Nature Phys. 15 (2019) 1113, 10.1038/s41567-019-0611-8
10. D. Everett et al., Multisystem Bayesian constraints on the transport coefficients of QCD matter, Phys. Rev. C 103 (2021) 054904, 10.1103/PhysRevC.103.054904
11. Elliptic flow of charged particles at midrapidity relative to the spectator plane in Pb-Pb and Xe-Xe collisions (2022), <https://doi.org/10.48550/arXiv.2204.10240>
12. S. Gavin and M. Abdel-Aziz, Measuring Shear Viscosity Using Transverse Momentum Correlations in Relativistic Nuclear Collisions, Phys. Rev. Lett. 97 (2006) 162302, 10.1103/PhysRevLett.97.162302
13. M. Sharma and C. A. Pruneau, Methods for the Study of Transverse Momentum Differential Correlations, Phys. Rev. C 79 (2009) 024905, 10.1103/PhysRevC.79.024905
14. H. Agakishiev et al., Evolution of the differential transverse momentum correlation function with centrality in Au+Au collisions at  $\sqrt{s_{NN}} = 200$  GeV, Phys. Lett. B 704 (2011) 467, 10.1016/j.physletb.2011.09.075
15. S. Acharya et al., Longitudinal and azimuthal evolution of two-particle transverse momentum correlations in Pb-Pb collisions at  $\sqrt{s_{NN}} = 2.76$  TeV, Phys. Lett. B 804 (2020) 135375, 10.1016/j.physletb.2020.135375

16. Two-particle transverse momentum correlations in pp and p-Pb collisions at LHC energies (2022), <https://doi.org/10.48550/arXiv.2211.08979>
17. V. Gonzalez, et al., Extraction of the specific shear viscosity of quark-gluon plasma from two-particle transverse momentum correlations, *Eur. Phys. J. C* 81 (2021) 465, [10.1140/epjc/s10052-021-09260-z](https://doi.org/10.1140/epjc/s10052-021-09260-z)
18. R. Rapp, Dilepton Spectroscopy of QCD Matter at Collider Energies, *Adv. High Energy Phys.* 2013 (2013) 148253, [10.1155/2013/148253](https://doi.org/10.1155/2013/148253)
19. T. Song, et al., Open charm and dileptons from relativistic heavy-ion collisions, *Phys. Rev. C* 97 (2018) 064907, [10.1103/PhysRevC.97.064907](https://doi.org/10.1103/PhysRevC.97.064907)
20. S. Acharya et al., Measurement of electrons from semileptonic heavy-flavour hadron decays at midrapidity in pp and Pb-Pb collisions at  $\sqrt{s_{NN}} = 5.02$  TeV, *Phys. Lett. B* 804 (2020) 135377, [10.1016/j.physletb.2020.135377](https://doi.org/10.1016/j.physletb.2020.135377)
21. S. Acharya et al., Direct photon production at low transverse momentum in proton-proton collisions at  $\sqrt{s} = 2.76$  and 8 TeV, *Phys. Rev. C* 99 (2019) 024912, [10.1103/PhysRevC.99.024912](https://doi.org/10.1103/PhysRevC.99.024912)
22. C. Gale, et al., Multimessenger heavy-ion collision physics, *Phys. Rev. C* 105 (2022) 014909, [10.1103/PhysRevC.105.014909](https://doi.org/10.1103/PhysRevC.105.014909)
23. H. van Hees, M. He, and R. Rapp, Pseudo-critical enhancement of thermal photons in relativistic heavy-ion collisions?, *Nucl. Phys. A* 933 (2015) 256, [10.1016/j.nuclphysa.2014.09.009](https://doi.org/10.1016/j.nuclphysa.2014.09.009)
24. J.-F. Paquet, et al., Production of photons in relativistic heavy-ion collisions, *Phys. Rev. C* 93 (2016) 044906, [10.1103/PhysRevC.93.044906](https://doi.org/10.1103/PhysRevC.93.044906)
25. R. Chatterjee, et al., Collision centrality and  $\tau_0$  dependence of the emission of thermal photons from fluctuating initial state in ideal hydrodynamic calculation, *Phys. Rev. C* 85 (2012) 064910, [10.1103/PhysRevC.85.064910](https://doi.org/10.1103/PhysRevC.85.064910)
26. R. Chatterjee, L. Bhattacharya, and D. K. Srivastava, Electromagnetic probes, *Lect. Notes Phys.* 785 (2010) 219, [10.1007/978-3-642-02286-9\\_7](https://doi.org/10.1007/978-3-642-02286-9_7)
27. O. Linnyk, et al., Hadronic and partonic sources of direct photons in relativistic heavy-ion collisions, *Phys. Rev. C* 92 (2015) 054914, [10.1103/PhysRevC.92.054914](https://doi.org/10.1103/PhysRevC.92.054914)
28. M. He, R. J. Fries, and R. Rapp, Ideal Hydrodynamics for Bulk and Multistrange Hadrons in  $\sqrt{s_{NN}}=200$  AGeV Au-Au Collisions, *Phys. Rev. C* 85 (2012) 044911, [10.1103/PhysRevC.85.044911](https://doi.org/10.1103/PhysRevC.85.044911)
29. N. P. M. Holt, P. M. Hohler, and R. Rapp, Thermal photon emission from the  $\pi\rho\omega$  system, *Nucl. Phys. A* 945 (2016) 1, [10.1016/j.nuclphysa.2015.09.008](https://doi.org/10.1016/j.nuclphysa.2015.09.008)
30. M. Heffernan, P. Hohler, and R. Rapp, Universal Parametrization of Thermal Photon Rates in Hadronic Matter, *Phys. Rev. C* 91 (2015) 027902, [10.1103/PhysRevC.91.027902](https://doi.org/10.1103/PhysRevC.91.027902)
31. S. Turbide, R. Rapp, and C. Gale, Hadronic production of thermal photons, *Phys. Rev. C* 69 (2004) 014903, [10.1103/PhysRevC.69.014903](https://doi.org/10.1103/PhysRevC.69.014903)
32. T. Matsui and H. Satz,  $J/\psi$  Suppression by Quark-Gluon Plasma Formation, *Phys. Lett. B* 178 (1986) 416, [10.1016/0370-2693\(86\)91404-8](https://doi.org/10.1016/0370-2693(86)91404-8)
33. S. Acharya et al., Measurements of inclusive  $J/\psi$  production at midrapidity and forward rapidity in Pb-Pb collisions at  $\sqrt{s_{NN}} = 5.02$  TeV (2023), <https://doi.org/10.48550/arXiv.2303.13361>
34. A. Andronic, et al., Transverse momentum distributions of charmonium states with the statistical hadronization model, *Phys. Lett. B* 797 (2019) 134836, [10.1016/j.physletb.2019.134836](https://doi.org/10.1016/j.physletb.2019.134836)
35. X. Du and R. Rapp, Sequential Regeneration of Charmonia in Heavy-Ion Collisions, *Nucl. Phys. A* 943 (2015) 147, [10.1016/j.nuclphysa.2015.09.006](https://doi.org/10.1016/j.nuclphysa.2015.09.006)
36. P. Braun-Munzinger and J. Stachel, (Non)thermal aspects of charmonium production and a new look at  $J/\psi$  suppression, *Phys. Lett. B* 490 (2000) 196, [10.1016/S0370-2693\(00\)00991-6](https://doi.org/10.1016/S0370-2693(00)00991-6)
37. R. L. Thews, M. Schroedter, and J. Rafelski, Enhanced  $J/\psi$  production in deconfined quark matter, *Phys. Rev. C* 63 (2001) 054905, [10.1103/PhysRevC.63.054905](https://doi.org/10.1103/PhysRevC.63.054905)
38. P. Braun-Munzinger and J. Stachel, The quest for the quark-gluon plasma, *Nature* 448 (2007) 302, [10.1038/nature06080](https://doi.org/10.1038/nature06080)
39.  $\psi(2S)$  suppression in Pb-Pb collisions at the LHC (2022), <https://doi.org/10.48550/arXiv.2210.08893>
40. S. Acharya et al., Prompt  $D^0$ ,  $D^+$ , and  $D^{*+}$  production in Pb-Pb collisions at  $\sqrt{s_{NN}} = 5.02$  TeV, *JHEP* 01 (2022) 174, [10.1007/JHEP01\(2022\)174](https://doi.org/10.1007/JHEP01(2022)174)
41. Measurement of the radius dependence of charged-particle jet suppression in Pb-Pb collisions at  $\sqrt{s_{NN}} = 5.02$  TeV (2023), <https://doi.org/10.48550/arXiv.2303.00592>
42. Z. Citron et al., Report from Working Group 5: Future physics opportunities for high-density QCD at the LHC with heavy-ion and proton beams, *CERN Yellow Rep. Monogr.* 7 (2019) 1159, [10.23731/CYRM-2019-007.1159](https://doi.org/10.23731/CYRM-2019-007.1159)
43. ALICE upgrades during the LHC Long Shutdown 2 (2023), <https://doi.org/10.48550/arXiv.2302.01238>
44. Letter of Intent: A Forward Calorimeter (FoCal) in the ALICE experiment, *Tech. rep.*, CERN, Geneva (2020), URL <https://cds.cern.ch/record/2719928>.
45. L. Musa, Letter of Intent for an ALICE ITS Upgrade in LS3, *Tech. rep.*, CERN, Geneva (2019), [10.17181/CERN-LHCC-2019-018](https://doi.org/10.17181/CERN-LHCC-2019-018), URL <https://cds.cern.ch/record/2703140>.
46. D. Adamová et al., A next-generation LHC heavy-ion experiment (2019), <https://doi.org/10.48550/arXiv.1902.01211>
47. Letter of intent for ALICE 3: A next-generation heavy-ion experiment at the LHC (2022), <https://doi.org/10.48550/arXiv.2211.02491>
48. P. M. Hohler and R. Rapp, Is  $\rho$ -Meson Melting Compatible with Chiral Restoration?, *Phys. Lett. B* 731 (2014) 103, [10.1016/j.physletb.2014.02.021](https://doi.org/10.1016/j.physletb.2014.02.021)
49. A. Rothkopf, Heavy Quarkonium in Extreme Conditions, *Phys. Rept.* 858 (2020) 1, [10.1016/j.physrep.2020.02.006](https://doi.org/10.1016/j.physrep.2020.02.006)